ACS SENSORS

pubs.acs.org/acssensors Article

Smart Contact Lens with High Sensitivity and Biocompatibility for Continuous Non-Invasive Intraocular Pressure Monitoring

Yunhao Tai, Qilong Cheng, Yuteng Liu, Xingqi Lu, Ting Xu, Xiaojian Li, Ping Liu, Tingting Luo,* Guangli Liu,* Yijing Gan,* and Runhuai Yang*

Cite This: https://doi.org/10.1021/acssensors.5c00883 Read Online

ACCESS | Metrics & More | Article Recommendations | Supporting Information

ABSTRACT: Intelligent intraocular pressure (IOP) sensors capable of continuous monitoring play a crucial role in the treatment of glaucoma. However, early diagnosis and treatment continue to face significant challenges due to the unique physiological environment of the eye. The primary scientific challenge lies in developing a method for continuous, high-sensitivity IOP monitoring that does not damage corneal tissue. To address this issue, a novel smart contact lens was developed, integrating hydrogel-based micronano architectures with diffraction-grating-embedded films. This device leverages 3D printing technology to achieve conformal adhesion to the ocular surface, enabling real-time IOP monitoring through optical-to-digital signal transduction. Additionally, ex vivo porcine eyeballs were used for in vitro testing and evaluation to quantitatively demonstrate the performance of the smart sensor. The results indicate that the smart contact lens developed in this study exhibits excellent biocompatibility and a high sensitivity of 2.5% $mmHg^{-1}$ within the range of 0–50 mmHg, enabling precise IOP monitoring. These lenses hold significant potential for clinical IOP monitoring and demonstrate substantial promise for the next generation of ocular disease prevention.

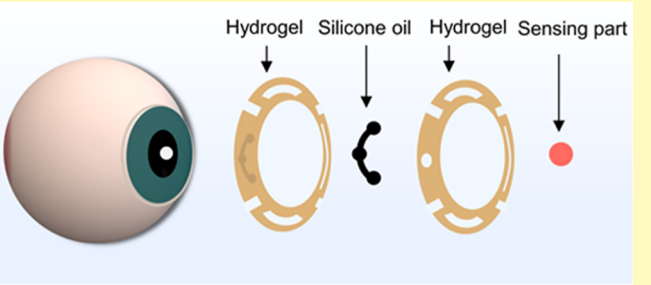

KEYWORDS: *smart contact lens, intraocular pressure monitoring, stress collection, 3D printing, biocompatibility*

Glaucoma, as the second leading cause of blindness globally, often leads to irreversible blindness. It is estimated to affect over 80 million people in 2024 and is projected to increase to 118 million by 2040.[1,2] However, due to the slow onset of glaucoma symptoms, early diagnosis and treatment remain a significant challenge.[3−5] Consequently, early detection of glaucoma and taking preventive measures are crucial.[6,7] In this regard, elevated IOP is generally considered a primary indicator of glaucoma,[8−11] and continuous monitoring and timely treatment can reduce the threat to vision of glaucoma. Although various types of tonometers, such as the Goldmann applanation tonometer, noncontact tonometer, rebound tonometer, and dynamic contour tonometer, are clinically used for IOP monitoring,[12−15] these tonometers can only provide a single measurement result and cannot monitor IOP fluctuations in real-time.[16,17] In addition, due to factors such as positional changes and circadian rhythms,[18,19] it is difficult to obtain accurate IOP values during clinical visits, making it challenging to develop appropriate treatment plans.[20] The bottleneck that causes these challenges is how to achieve continuous noninvasive monitoring of IOP.

To enable noninvasive monitoring of dynamic IOP changes, wearable smart IOP sensors have emerged. By integrating a variety of electronic sensors, microprocessors, and display components, these devices enable continuous and noninvasive IOP monitoring,[21,22] which is crucial for the prevention and treatment of glaucoma. For instance, combining contact lenses with inductor-capacitor-resistor (LCR) resonators[23−25] can effectively address the challenge of continuous IOP monitoring at night, demonstrating practical application potential. The integration of deep learning architectures with sensor technologies, employing big data-trained predictive models for IOP identification and classification, has emerged as a novel monitoring paradigm.[26,27] This innovative methodology demonstrates significant potential in ophthalmological diagnostics through its exceptional data-processing capacity, enabling high-precision measurement capabilities. The system's advanced computational framework facilitates accurate and reliable IOP measurements with enhanced sensitivity and specificity compared to conventional monitoring approaches. Additionally, with the rapid development of materials science, two-dimensional (2D) material graphene[28,29] has also been applied in IOP sensors. Combining it with external circuits can

Received: March 17, 2025
Revised: May 17, 2025
Accepted: June 16, 2025

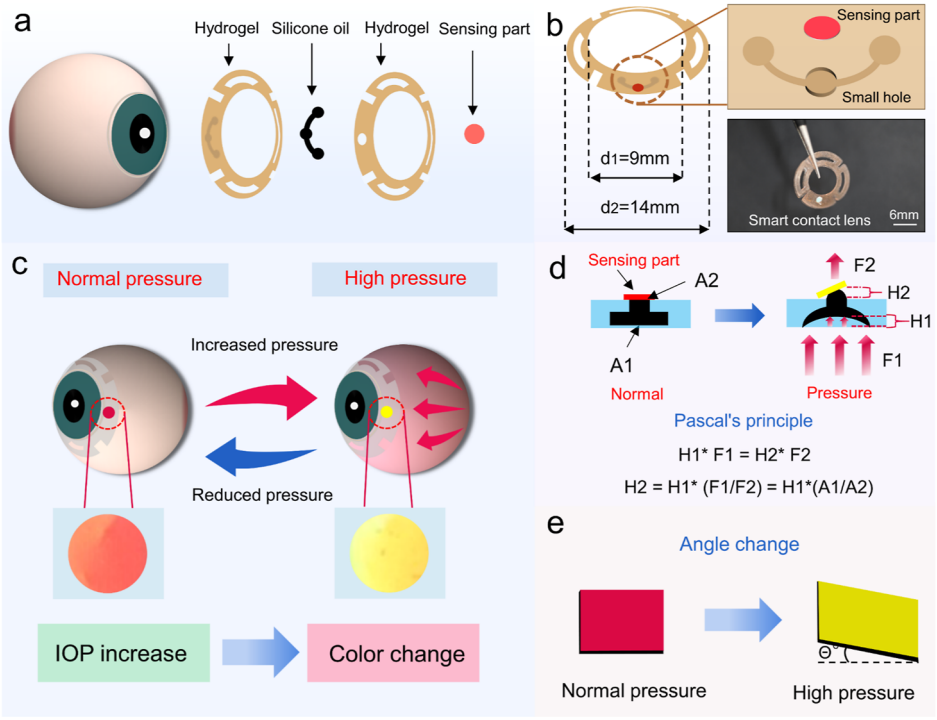

Figure 1. Principles and design of the smart sensor for IOP monitoring. (a) Schematic diagram of the hierarchical structure of the smart IOP sensor. (b) Design and physical image of the smart IOP sensor. (c) Schematic illustration of the working principle of the smart IOP sensor. (d) Schematic diagram of the corneal stress collection structure based on Pascal's principle. (e) Schematic illustration of the working principle of the grating membrane.

improve the accuracy and sensitivity of IOP monitoring.[26,30] However, these monitoring methods require additional power sources and wiring connections,[31,32] which may cause corneal damage during long-term wear[33,34] and pose challenges to comfort and practicality during continuous IOP monitoring.[35] Consequently, the development of an IOP sensor solution that is nondamaging to the cornea, highly sensitive, and capable of real-time monitoring, along with a corresponding integrated manufacturing method, is of great significance for human IOP monitoring.

Facing the above-mentioned challenges, we propose a design strategy for an IOP sensor that combines hydrogel micronano structures with a diffraction grating film. Based on this strategy, we developed a smart contact lens using 3D printing manufacturing methods. This contact lens continuously measures IOP values by utilizing the color change of a diffraction-based grating film pressure sensor, without requiring complex wiring and measurement equipment, thus avoiding corneal damage. As the grating film pressure sensor changes its reflected wavelength with increasing IOP, different color changes can be observed at a fixed position. Using 3D printing, it is convenient to manufacture smart contact lenses with micronano structures that adaptively fit the shape of the eyeball, enabling personalized customization while also achieving high sensitivity of 2.5% $mmHg^{-1}$. In addition, the use of poly(ethylene glycol) diacrylate (PEGDA) cross-linked with acrylamide (AM) to form a double-network (P-DN) hydrogel as a bioink for 3D printing allows for a gentle fabrication process with low cost while maintaining excellent biocompatibility, providing a possibility for continuous and noninvasive IOP monitoring.

RESULTS AND DISCUSSION

Design and Working Principle of the Smart Contact Lens. To enhance the monitoring and collection of IOP signals, we designed the smart IOP sensor to consist of two components: a microfluidic ring (contact part) and a diffraction grating membrane (sensing part). As shown in Figure 1a, the center of our smart IOP sensor is hollow, so the optical transparency is almost unaffected by the assembly of the two layers. The main body of the contact part is made of P-DN hydrogel, with high-viscosity silicone oil sealed in the middle, and a diffraction grating membrane covering the small holes on the outermost layer. According to previous studies, the maximum deformation of the cornea occurs 5 mm from the center of the cornea, called the corneal and scleral junction,[29] so our microfluidic channels are also attached here. As shown in Figure 1b, the inner diameter of the annular channel is 9 mm, and the outer diameter is 14 mm, which can perfectly cover the limbus.

Figure 1c illustrates the working principle and structural schematic diagram of the smart IOP sensor, which demonstrates distinct color changes in the sensing part under varying IOP conditions. Figure 1d presents a schematic diagram of the working principle of Pascal's law, which amplifies the deformation caused by pressure at the bottom due to the difference in membrane areas at the bottom and top of the convex chamber. According to Pascal's principle, the deformation of the smart IOP sensor is amplified as follows

$$H_2 = H_1 * \left(\frac{A_1}{A_2}\right) \quad (1)$$

In this equation, H_2 and H_1 represent the vertical deformation of the grating membrane (sensing part) and the hydrogel

https://doi.org/10.1021/acssensors.5c00883
ACS Sens. XXXX, XXX, XXX−XXX

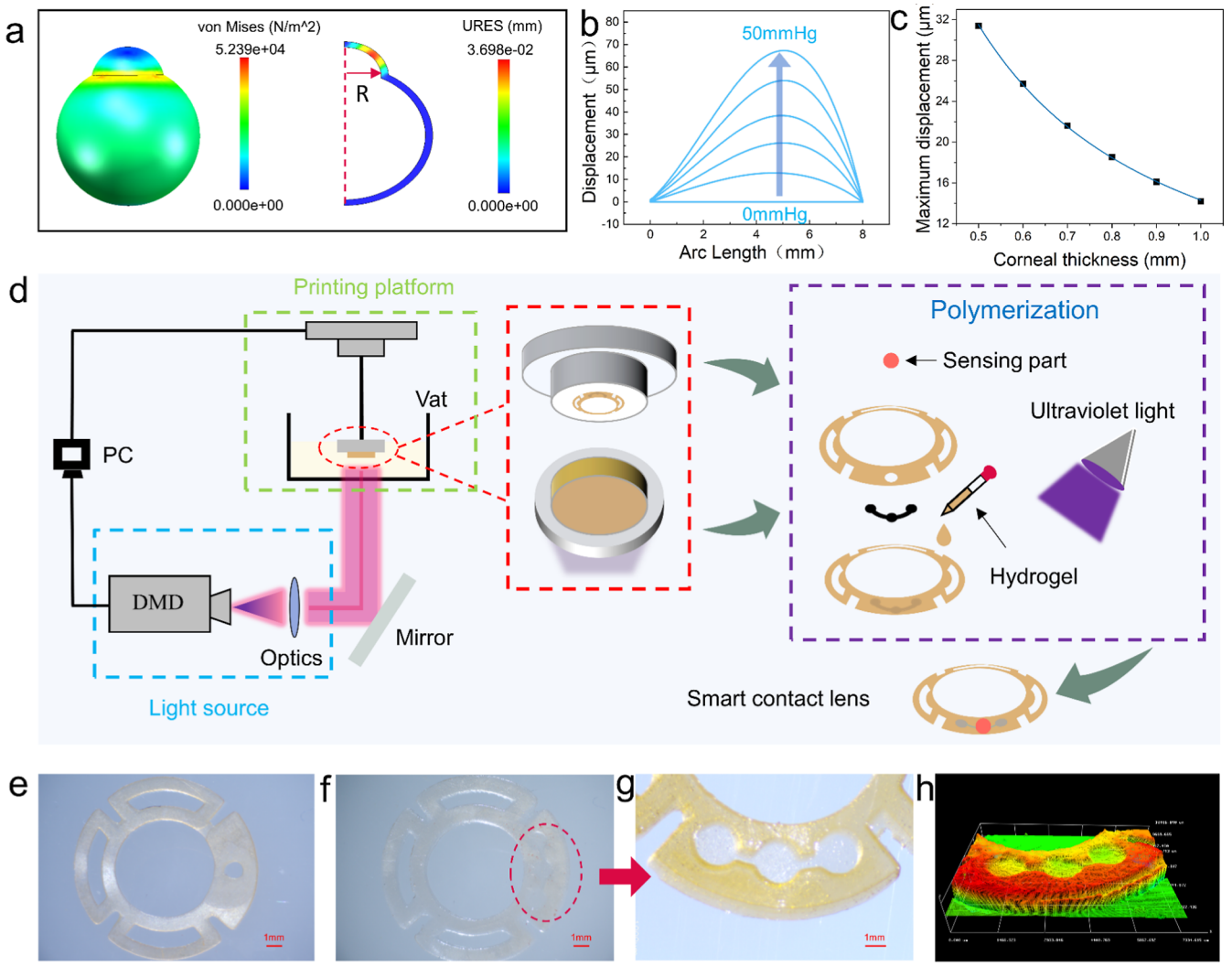

Figure 2. Simulation and design of the sensor. (a) Simulation of surface stress distribution on the eyeball under the influence of IOP. (b) Relationship between corneal base curve deformation and IOP along the *R*-direction. (c) Illustration of maximum corneal deformation for corneas of varying thicknesses under identical pressure conditions. (d) Description of the fabrication process for the smart IOP sensor. (e) Photograph of the top membrane of the sensing section. (f) Photograph of the bottom membrane of the sensing section. (g) Schematic of the microfluidic design for collecting corneal stress. (h) Three-dimensional structural diagram of the microfluidic system.

membrane (contact part), respectively, and A_2 and A_1 are the membrane areas within the grating membrane and hydrogel membrane, respectively. Consequently, the sensor deformation can be estimated by the area ratio of the two membranes. However, given that our microfluidic structure comprises three cylindrical chambers, the amplification factor should be three times the original amplification, with the specific formula detailed as follows

$$H_2 = 3H_1 * \left(\frac{A_1}{A_2}\right) \quad (2)$$

Consequently, stress on the cornea can be collected through the design of microstructures, thereby amplifying the corneal deformation. Additionally, for the sensing part, we use a diffraction-based grating membrane. Due to the amplification of corneal deformation by the contact part, the sensing part changes its original position, resulting in different color changes, as shown in Figure 1e.

Simulation and Fabrication of the Smart Contact Lens. Fluctuations in IOP induce corneal deformation, and previous in vivo and ex vivo studies have indicated that a 1 mmHg change in IOP results in a central corneal curvature radius change of approximately 3 μm.[36] When IOP increases, deformation occurs uniformly across the cornea, with the most significant changes primarily at the corneoscleral junction.[37,38] We employed finite element simulation to model the distribution of stress and deformation in the eye under the influence of IOP. Given that the sclera has a much higher elastic modulus than the cornea,[29] the majority of deformation is concentrated in the corneal region,[39] as shown in Figure 2a. Additionally, due to the nonuniform thickness of the cornea, its deformation is also nonuniform, predominantly distributed from the corneal center to the corneoscleral junction.[40] In cross-section, we calculated the deformation of the corneal base curve along the *R*-direction (radial direction) with respect to IOP. As IOP increases, the extent of deformation becomes more widespread, reaching a peak at a distance of 5 mm from the center of the cornea (Figure 2b). In addition, due to individual variability, the corneal thickness varies among different eyes. Figure 2c depicts the maximum corneal deformation under the same IOP for eyes with different

https://doi.org/10.1021/acssensors.5c00883
ACS Sens. XXXX, XXX, XXX−XXX

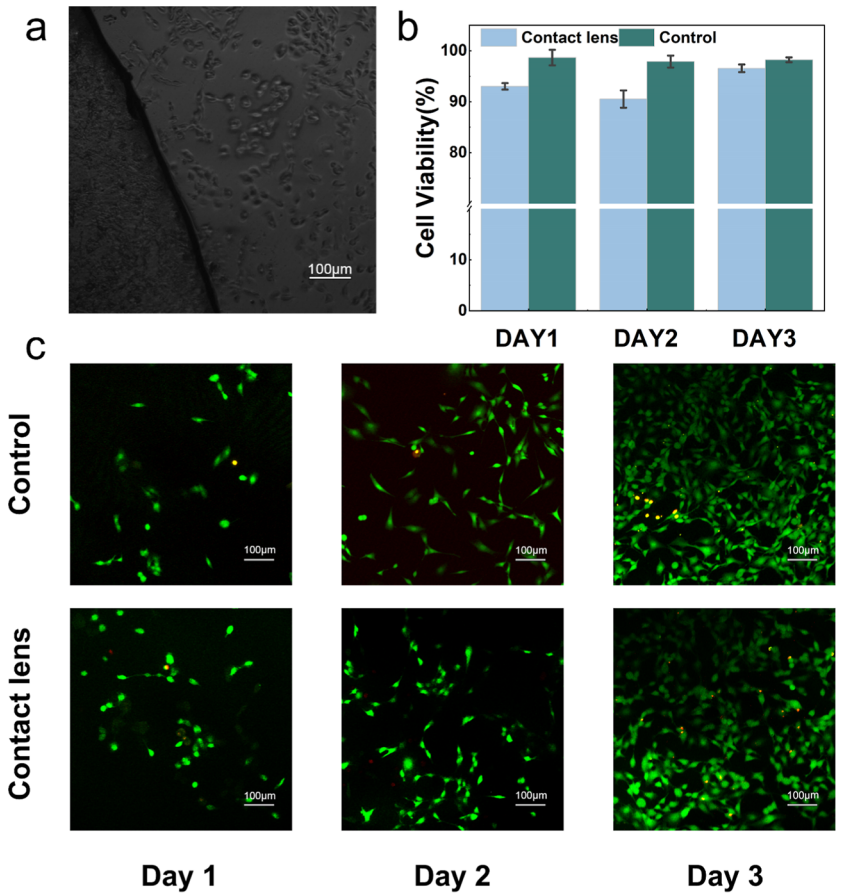

Figure 3. Biocompatibility of P-DN Hydrogel. (a) Confocal micrograph of coculture of cells and P-DN hydrogel (scale bar: 100 μm). (b) Viability of Saos-2 cells after 3 days of coculture with P-DN hydrogel. (c) Live/dead staining images of Saos-2 cells (scale bar: 100 μm).

corneal thicknesses. With increasing corneal thickness, the cornea's sensitivity to force decreases, and thus the maximum deformation also diminishes.[28,29]

Based on the aforementioned simulation results, we utilized a digital light processing (DLP) printer to fabricate the smart IOP sensor. Figure 2d depicts the primary manufacturing process of the smart IOP sensor. The detailed description of the whole procedure can be found in the Experimental Section. In brief, the designed model was sliced and printed using a DLP 3D printer (Figure S1). Figure 2e,f display the structures of the top and bottom membranes, respectively. The top layer membrane primarily retains a small hole, while the bottom hydrogel flexible membrane has three cylindrical chambers in communication, with the microstructure shown in Figure 2g. Figure 2h presents the three-dimensional model of the microfluidic structure. Subsequently, high-viscosity silicone oil was encapsulated within the microfluidic structure, and the entire assembly was polymerized under external UV light exposure. The small hole on the hydrogel flexible membrane was covered with the sensing part, a grating membrane. Compared to the fabrication methods of other IOP sensors, our approach is more gentle, convenient, and imposes less stress on the device. In addition, through the design of the overall structure, our smart contact lens can conform adaptively to the human corneal surface (Figure S2) without detaching from the cornea during long-term monitoring.

Biocompatibility Assessment of Smart Contact Lens. Given the direct contact of P-DN hydrogel with the human eye, ensuring the exceptional biocompatibility of the smart contact lens is imperative. To validate this biocompatibility,[23] P-DN hydrogel samples were cocultured with human osteosarcoma cells (Saos-2)[41] in a shared medium for 3 days, followed by measurement of cell density after calcein AM/PI staining. The control group was processed identically to the experimental group except for the absence of the sample. Figure 3a presents the differential interference contrast images of the P-DN hydrogel in coculture with cells, facilitating a visual assessment of the hydrogel's biocompatibility. Cell viability was comprehensively evaluated by enumerating dead and live cells and calculating viability across three distinct areas over the three-day period, utilizing ImageJ NIH software (Figure 3b). Normal cell morphology observed throughout the three-day culture period indicated sustained cell viability. Cell density measurements after calcein AM/PI staining revealed that both the experimental and control groups predominantly consisted of live cells (Figure 3c). The statistical analysis indicated no significant differences in cell viability between the contact lens group and the control group. Additionally, the survival rate of all cells cocultured with P-DN hydrogel exceeded 90%. Live/dead staining revealed a uniform distribution of green-stained live cells in the culture medium, exhibiting good condition, regular morphology, and uniform size, with no significant signs of apoptosis or necrosis observed. Quantitative analysis indicated no significant decrease in cell numbers on the second and third days compared to the first day, and no significant differences were observed compared to the control group, demonstrating the superior biocompatibility of P-DN hydrogel.

https://doi.org/10.1021/acssensors.5c00883
ACS Sens. XXXX, XXX, XXX−XXX

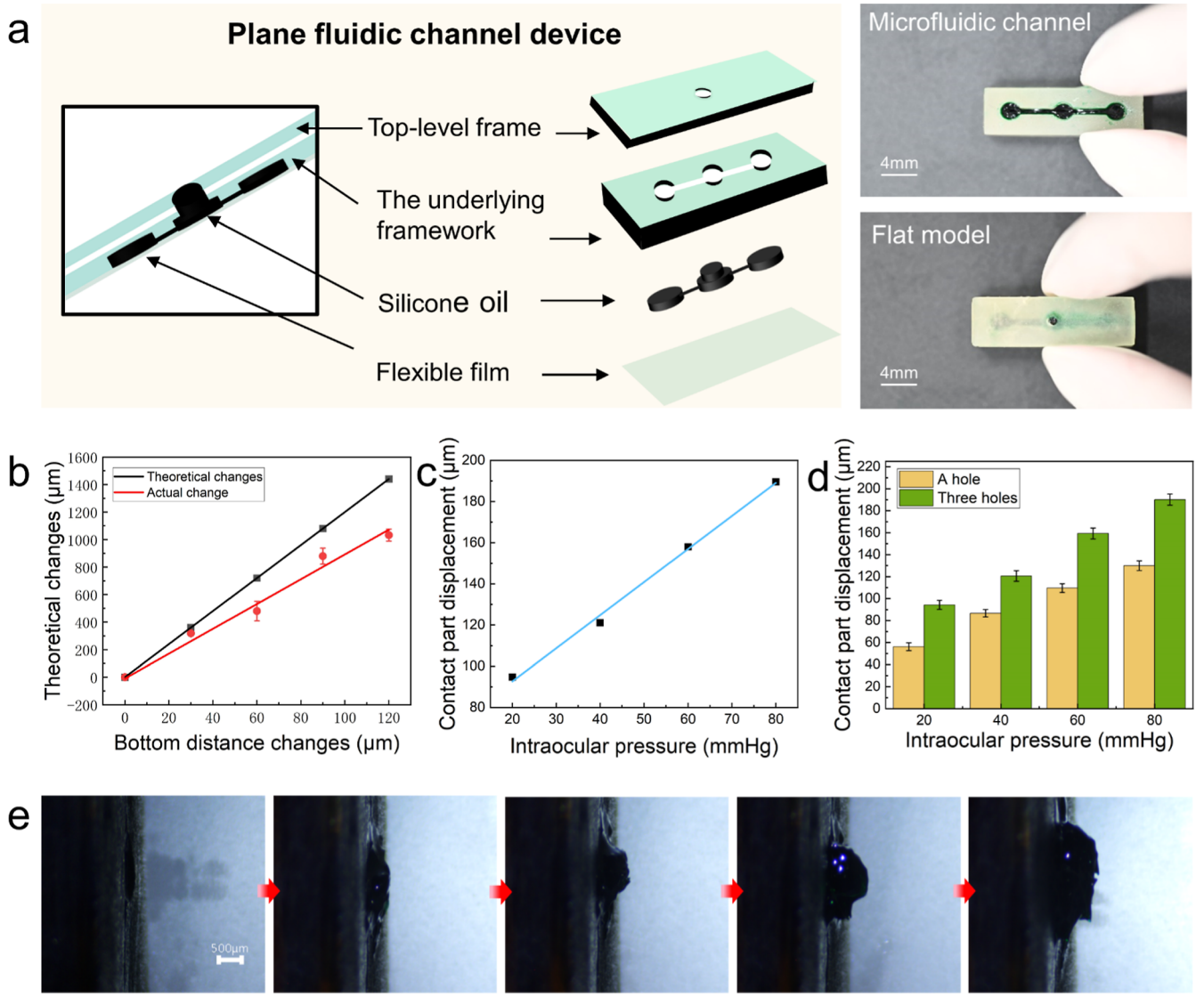

Figure 4. Investigation of Corneal Stress Collection Using a Planar Fluidic Channel Device. (a) Schematic and physical images depicting the hierarchical structure of the planar fluidic channel device. (b) Comparison between the theoretical and actual values of the expanded volume at the top when the same volume change occurs at the bottom of the fluid. (c) Illustration of the linear relationship between pressure and the expansion of the contact area. (d) Comparison of the expansion of the contact area under the same pressure change between a single-chamber and a triple-chamber configuration. (e) Physical images showing the expansion of the contact area when the fluid volume is quantitatively altered.

Investigation of the Corneal Stress Collection System. To evaluate the performance of the microfluidic amplification system for collecting corneal stress with smart contact lenses, we designed a "plane fluidic channel device" with an identical structure to the contact portion of the smart contact lens. The fluid within this device, high-viscosity silicone oil, is sealed by a flexible membrane made of PEGDA hydrogel. Given the requirement for long-term IOP monitoring using an IOP sensor, it is crucial to ensure that the sensor remains undamaged throughout the process. If a liquid with higher fluidity is utilized as the filling liquid, it may flow out due to factors such as gravity during the monitoring process, leading to experimental errors.[4] Conversely, high-viscosity silicone oil can remain within the microfluidic chamber channel, thereby reducing experimental errors and ensuring the repeatability of the sensor.[42] Figure 4a presents both a schematic and a physical image of the planar fluidic channel device. The device amplifies the deformation of the fluid within the microfluidic channels through external stimulation applied to the bottom, leveraging Pascal's principle for amplification. To quantitatively verify the amplification performance of Pascal's principle, we varied the fluid volume and recorded the amplified volume changes as shown in Figure 4e.

Figure 4b illustrates the comparison between the theoretical and actual values of the amplified volume when changes occur at the bottom of the fluid. Additionally, we validated the volume changes in the contact portion under different pressures applied to the bottom of the flexible membrane, as depicted in Figure 4c. The measured actual values were lower than the theoretical values during the experiment, which can be attributed to the fact that the amplification mechanism in Pascal's principle is based on a frictionless fluid within an ideal cylindrical model, whereas our cylindrical chambers are structurally smaller. Additionally, the fluid is influenced by the length of the microfluidic channels and the viscosity of the

https://doi.org/10.1021/acssensors.5c00883
ACS Sens. XXXX, XXX, XXX−XXX

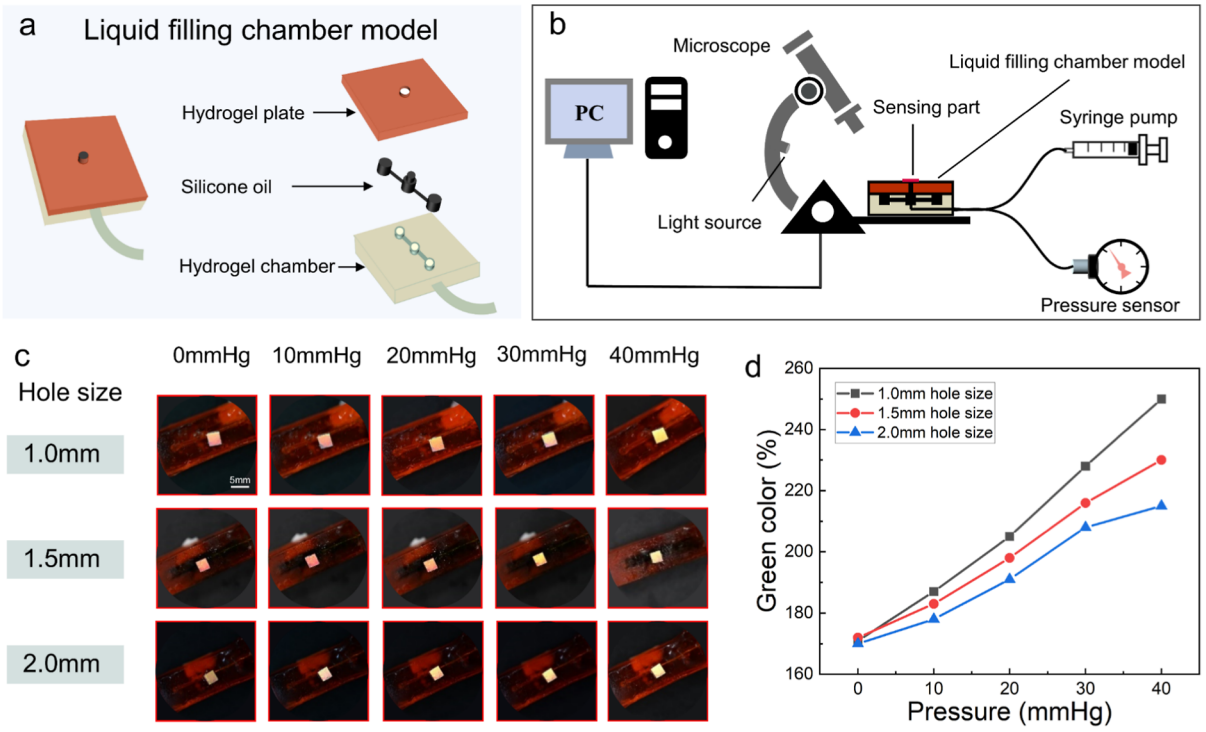

Figure 5. Optimization of aperture diameter in the sensing component. (a) Schematic diagram representing the layered structure of the liquid filling device. (b) Experimental setup diagram investigating the variation in the *G*-value of the grating membrane. (c) Graph illustrating the color changes of the grating membrane across different apertures in response to pressure changes. (d) Plot demonstrating the *G*-value changes for different apertures over the same range of pressure variations.

fluid itself, which may reduce the stress experienced by the bottom flexible membrane.[4] Since an increase in aqueous humor exerts stress uniformly across the cornea, our microfluidic channels are designed to connect three cylindrical chambers. When subjected to stress, the fluid within all three cylindrical chambers deforms and is transported through the central microfluidic channel to the middle chamber, from where it is expelled through the small opening at the top, thereby collecting and amplifying the stress. Figure 4d demonstrates the amplification effect of one cylindrical chamber versus three cylindrical chambers under the same stress, clearly showing that the three-chamber configuration provides better amplification.

Geometric Design of the Optimal Amplification System. To achieve maximum deformation in the contact part, we explored the area ratios of cylindrical chambers. Initially, to determine the most appropriate aperture for the contact sensing part, we designed liquid filling chamber models with diameters of 1.0, 1.5, and 2.0 mm, covered with a sensing part grating membrane. Figure 5a illustrates the schematic of the liquid filling chamber model, where the base plate with a cylindrical chamber made of PEGDA hydrogel serves as the main part of the model, with the central chamber filled with silicone oil and the top hydrogel plate featuring circular holes of varying diameters. Figure 5b presents the experimental setup model for measuring the *G*-value of the contact part, with the specific experimental apparatus detailed in Figure S3. One end of the chamber was connected to a syringe pump and pressure gauge, enabling controlled injection of silicone oil to modulate internal pressure. Color changes in the sensing part under varying pressures were observed through a microscope fixed externally. Since the color change range is from red to yellow, we employed an RGB-based color analysis method. By comparing the *G*-value changes in the sensing part across the same pressure range for different apertures, we assessed the amplification effects of various apertures, as shown in Figure 5c.

Figure 5d depicts that the sensing part exhibited the greatest degree of color change at the smallest aperture. While the color change would be more pronounced with an aperture less than 1 mm, such small apertures are challenging to fabricate due to the limitations of hydrogel 3D printing and are too small for monitoring with the naked eye or a camera. Given our aim to measure IOP in a simple, cost-effective, and convenient manner, we determined that a 1.5 mm diameter aperture is the optimal size for the contact sensing part. In addition to exploring the aperture of the contact sensing part, we also investigated the optimal dimensions of the cylindrical chamber. We sought to determine the ideal cylindrical chamber to successfully create a smart contact lens with microfluidic stress collection and amplification capabilities (Figure S4). If silicone oil leaks from the microfluidic channel, it will prevent the manufacture of intelligent contact lenses with the correct amplification system. Experiments have shown that when high-viscosity silicone oil is injected into cylindrical chambers of different diameters, the oil does not flow out due to gravity when the chamber diameter is 2 mm. Furthermore, given the small size of the microfluidic structure, the high viscosity of the silicone oil, and the coverage of the grating film over the small holes, the produced intelligent contact lenses will not suffer from silicone oil leakage during long-term monitoring.

Exploration of the Initial Color Measurement. Given the limitations of obtaining precise information directly from the colors in the photographs, we performed CIELAB color space analysis. Figure 6a illustrates the spatial model of the CIELAB color space, enabling direct correlation of IOP values

https://doi.org/10.1021/acssensors.5c00883
ACS Sens. XXXX, XXX, XXX−XXX

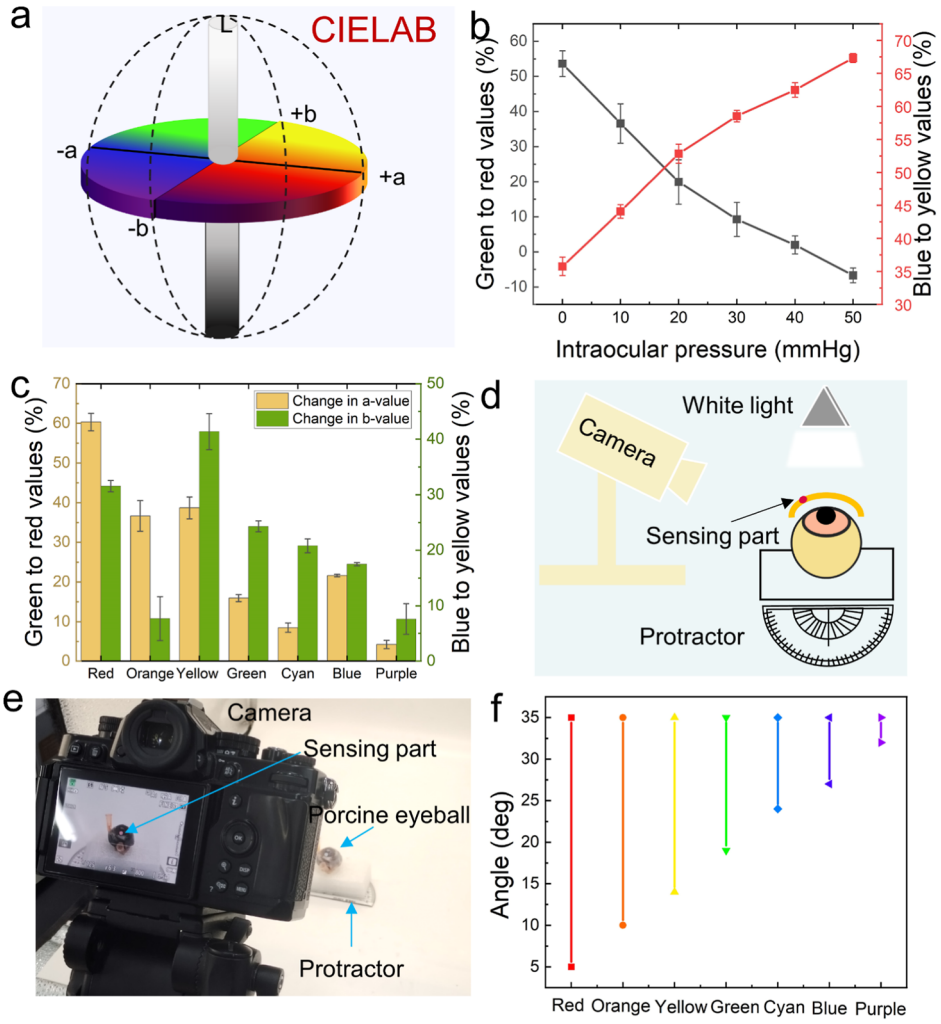

Figure 6. Determination of the initial measurement color. (a) Schematic illustration of the Lab color space. (b) Linear relationship between IOP and ab values when measurements are initiated from red. (c) Depiction of the range of ab value changes when measurements are initiated from different colors. (d) Schematic model of the device for determining the angular change range when measuring from different colors until no color change is observed. (e) Experimental setup for the angular change range. (f) Comparison of the angular change range when measuring from different colors until no color change is observed.

with ab chromaticity coordinates. This approach allowed for a precise one-to-one mapping between IOP measurements and color values, enhancing the accuracy of our color-based IOP assessments. In the initial stage of our experimental design, a predefined starting color for monitoring was not established. Consequently, we initiated measurements across seven distinct colors: red, orange, yellow, green, cyan, blue, and purple. This approach enabled us to evaluate color changes under consistent IOP variations. Subsequently, we conducted a Lab value analysis for each color and established a linear correlation between various IOP values and their corresponding ab values. This systematic methodology allowed for a rigorous scientific determination of the relationship between IOP and color changes. Figure 6b illustrates the variation in ab values when measurements are initiated from red within a 0−50 mmHg range. However, to ascertain the optimal starting color for monitoring, we also measured the sensor's response when initiated from six other colors: orange, yellow, green, cyan, blue, and purple (Figure S5), analyzing the ab value changes associated with transitions from these different colors. Figure 6c presents the range of ab value changes during monitoring initiated from various initial colors. It is evident from the figure that the greatest change in ab values occurs when monitoring starts from red, indicating that the highest sensitivity is achieved when red is the starting color.

To identify the color that provides the most extensive monitoring range, we analyzed the angular range of variation across different colors until no further color changes were detected. Figure 6d presents a model diagram of the testing apparatus, with the sensor applied to an ex vivo porcine eyeball, a protractor placed at the bottom. In tests on enucleated pig eyes, smart contact lenses were used under full illumination to ensure diffuse reflection, as shown in Figure S9. Under these conditions, environmental lighting and light source distance had minimal effects on the test. An externally fixed camera is used to record color changes, with the actual experimental setup shown in Figure 6e. Figure 6f illustrates the angular change from the seven colors—red, orange, yellow, green, cyan, blue, and purple—until no further color variation is detected. The results indicate that initiating the measurement from red provides a broader monitoring range, thus offering a potential approach for extensive IOP monitoring.

Since color changes could be monitored from various directions, we explored the optimal measurement angle.

https://doi.org/10.1021/acssensors.5c00883
ACS Sens. XXXX, XXX, XXX−XXX

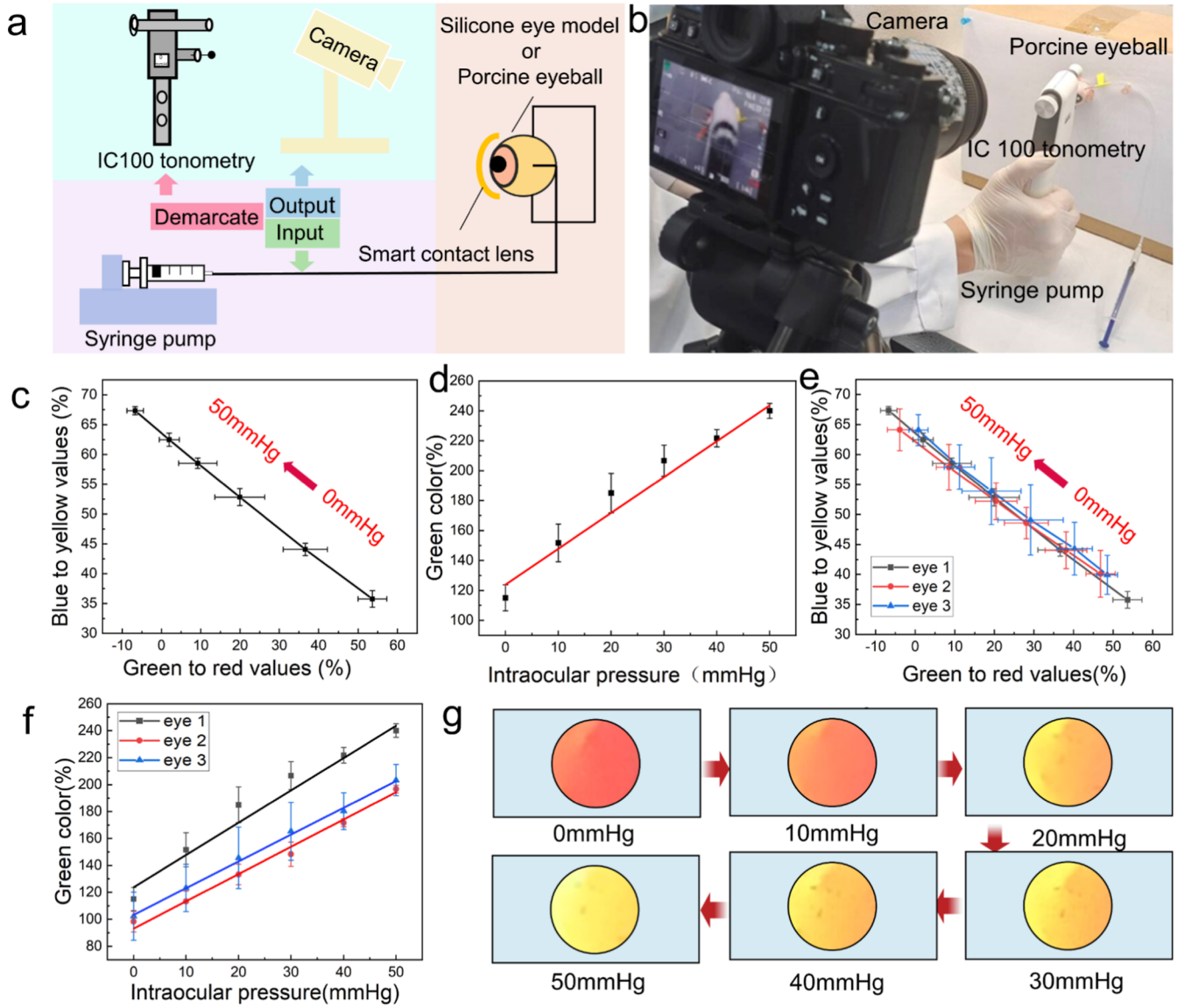

Figure 7. In vitro studies of the smart IOP sensor. (a) Schematic diagram of the ex vivo porcine eyeball monitoring model constructed. (b) Experimental setup for ex vivo porcine eyeball monitoring. (c) Illustration of the linear relationship between IOP values and ab values. (d) Representation of the linear relationship between IOP values and *G* values. (e) Linear relationship between IOP values and ab values in different ex vivo porcine eyeballs. (f) Linear relationship between IOP values and *G* values in different ex vivo porcine eyeballs. (g) Photographs of the smart IOP sensor's color changes under varying pressures.

Starting from a vertical angle of 0° between the camera and the smart contact lens, the grating film appeared red at a vertical angle of 35° and a horizontal angle of 10°, as well as at other angles listed in Figure S10. Additionally, we examined the horizontal angular range for the color shift from red to purple, as shown in Figure S11. A smaller angular range indicates a more sensitive sensor. For experimental convenience, the camera was fixed at a vertical angle of 50° and a horizontal angle of 0° relative to the smart contact lens, forming an integrated monitoring system to avoid measurement errors from different angles. During the experiment, the testing setup was fixed, so the camera parameters were also fixed. To ensure consistent results, the camera's ISO was set to 1000, the aperture to 2.8, and the shutter speed to 1/125. Since we used the ab values from the Lab color space for color analysis, and ISO only affects the *L* value, it did not impact the results. Additionally, due to environmental interference, the white balance during testing would change. Therefore, we tested the ab value variations of the grating film under different white balance conditions during identical color changes, as shown in Figure S12. Our analysis, presented in Figure S13, shows minimal differences in ab values across three white balance conditions, indicating a negligible effect of white balance on the results. To avoid environmental interference and enhance portability, we fixed the camera exposure parameters and light source intensity, and integrated the equipment into a portable tonometer, as shown in Figure S14. This minimizes the impact of parameter variations.

In Vitro Testing and Evaluation of the Smart Contact Lens. Given the similar biomechanical properties between porcine and human eyes,[43,44] we utilized ex vivo porcine eyeballs to assess the performance of our sensor. Figure 7a shows a schematic diagram of the pressure-controlled ex vivo porcine eyeball platform model that we constructed. The ex

https://doi.org/10.1021/acssensors.5c00883
ACS Sens. XXXX, XXX, XXX−XXX

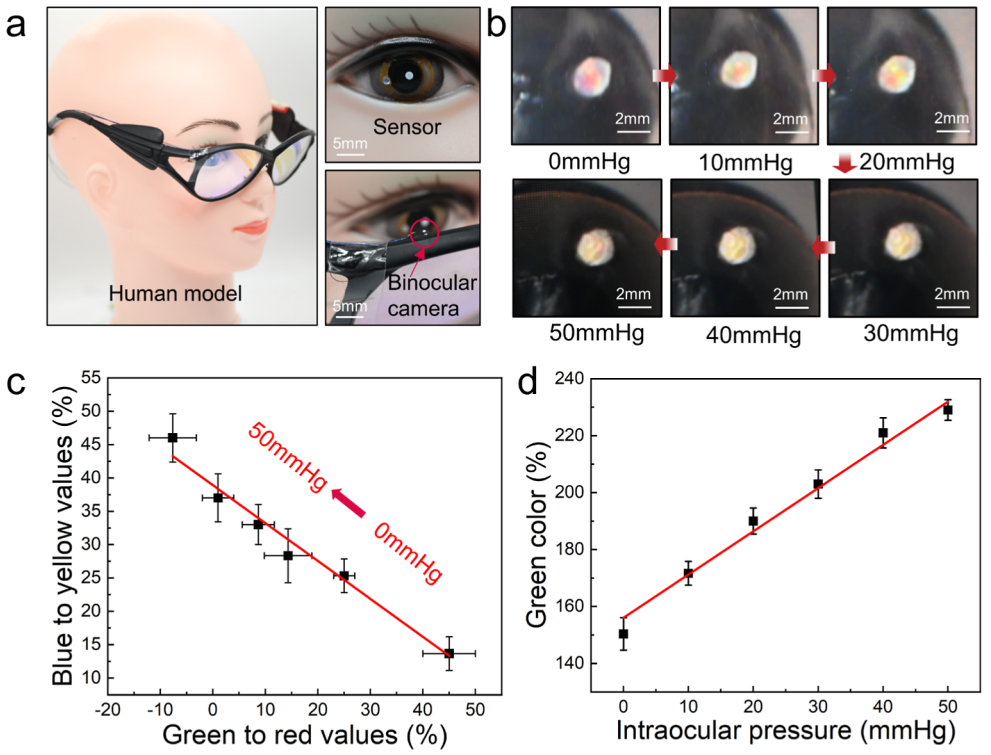

Figure 8. Remote reading of the smart contact lens. (a) Photograph of the integrated IOP monitoring system worn on a human model. (b) Images of the sensing component's color changes captured by the binocular camera under varying IOP conditions. (c) Illustration of the linear relationship between IOP values and ab values over a 0−50 mmHg range. (d) Depiction of the linear relationship between IOP values and *G* values within a 0−50 mmHg range.

vivo porcine eyeball, equipped with the smart contact lens, was vertically secured, and one end of a syringe pump was inserted into the porcine eyeball. The internal ocular pressure was controlled by injecting and aspirating deionized water. The iCare IC100 rebound tonometer was utilized for calibration to ascertain the specific IOP values. Once the IOP values were determined, a camera was used to document the color at that moment. Figure 7b illustrates the experimental setup. To ensure the physiological environment of the human eye is simulated, it is necessary to maintain a moist environment on the surface of the ex vivo porcine eyeball. Additionally, our smart contact lens possesses shape-adaptive functionality, preventing it from falling off during testing. Our smart contact lens successfully detected deformations under various IOP conditions, and by conducting color analysis on the photographed images (Figure 7g), we established a linear relationship between IOP values and ab values (Figure 7c). This finding suggests that initiating monitoring from red yields the broadest range of detection, thus offering potential for extensive IOP monitoring.

Prior studies have highlighted interindividual variations in IOP monitoring. To address this, we utilized a single IOP sensor to conduct experiments on three separate porcine eyeballs. Employing a consistent color analysis technique, we determined the linear correlations between varying IOP levels and the corresponding ab values and G values for the sensor across these eyes, as illustrated in Figure 7e,f. The findings indicate that our sensor exhibits a strong linear relationship across different eyes, which significantly mitigates the variability errors inherent in individual differences.

Remote Reading of the Integrated Smart Contact Lens. To facilitate continuous and convenient remote data acquisition for the smart contact lens,[45,46] we have integrated the IOP sensor, binocular camera, and glasses into a single, unified IOP monitoring system. This integration ensures streamlined data retrieval and enhances the practicality of our smart contact lens technology for extended IOP surveillance. Figure 8a shows a photograph of the integrated IOP monitoring system worn on a human model, demonstrating the ease with which the binocular camera can record color changes of the sensor. Additionally, the small size of the binocular camera (Figure S6) and its noncontact with the cornea reduce the likelihood of corneal damage during continuous monitoring. Figure 8b displays the various color changes of the sensor observed on an ex vivo porcine eyeball under different IOP conditions using the integrated smart contact lens, with a clear transition from red to yellow being observable. Based on the recorded color changes, a linear relationship between IOP values and ab values was analyzed (Figure 8c). Moreover, a comparative analysis between IOP values and *G* values was conducted, yielding a linear relationship as shown in Figure 8d. With these targeted designs, the integrated smart contact lens offers a convenient method for continuous IOP monitoring, providing a novel approach for clinical IOP surveillance.

CONCLUSIONS

In this study, we report on a smart contact lens with high sensitivity and biocompatibility for continuous, noninvasive IOP monitoring. We propose a strategy that synergizes hydrogel micronanostructures with diffraction grating-based films, leveraging 3D printing to conveniently manufacture smart contact lenses that adaptively conform to the ocular surface. These lenses exhibit a high sensitivity of 2.5%

https://doi.org/10.1021/acssensors.5c00883
ACS Sens. XXXX, XXX, XXX−XXX

$mmHg^{-1}$ and excellent biocompatibility. Additionally, they collect IOP-induced corneal deformations and amplify them through the design of micronanostructures, enhancing the changes in the grating membrane's sensing area and facilitating the conversion from IOP to color to digital values, thereby achieving real-time IOP monitoring. Consequently, this smart contact lens demonstrates significant potential as a monitoring system, providing critical warnings before high IOP causes damage to the eyes.

MATERIALS AND METHODS

Materials and Synthesis. A transparent solution was successfully prepared by blending 3 g of acrylamide (AM, 99.0%), 10 g of polyethylene glycol diacrylate (PEGDA, molec-ular weight 400), 0.1 g Irgacure 819, 0.01 g Sudan I, and 1 g deionized water. The detailed structural formula can be referenced in Figure S7. The mixture was subjected to magnetic stirring for a duration of 3 to 4 h, resulting in a homogeneous and clear solution.

Manufacture of Smart Contact Lenses. In the study, the contact section of the smart contact lens was manufactured via digital light processing (DLP) 3D printing. The model, incorporating micro- and nanostructural designs, was processed using slicing software (EFL-DLP) under the following parameters: light intensity of 4 mW/cm^2, a base layer exposure time of 2 s, a single layer exposure duration of 2 s, and a layer thickness set at 0.1 mm. The sliced model was subsequently loaded into the BP8600-DLP bioprinter, where UV irradiation initiated localized photopolymerization reactions, facilitating the precise, layer-by-layer fabrication of hydrogel structures. This printing sequence was completed within a minute. The sensor component of the smart contact lens was equipped with a grating membrane (JMT467), the surface topography of which is depicted in Figure S8. The grating membrane was procured from Jimeitu Company. The base membrane of the smart contact lens is 0.4 mm thick, circular, and has a diameter of 14 mm. The central hollow channel is also circular with a diameter of 9 mm. The external cut-out structure of the contact lens is rectangular, measuring 3 mm in length and 2 mm in width. The internal cut-out structure is formed by two circles with diameters of 11 mm and 13 mm. The top membrane of the smart contact lens is also designed to be circular, with a thickness of 0.4 mm and a diameter of 14 mm. The overall thickness of the contact lens is designed to be no more than 1 mm.

Biocompatibility Tests. Human osteosarcoma cells (Saos-2) were maintained in Dulbecco's modified eagle medium (DMEM) supplemented with 10% fetal bovine serum (FBS) and subsequently seeded into 35 mm confocal dishes with a glass bottom diameter of 15 mm. The cells were incubated at 37 °C in a 5% CO_2 atm within a cell culture incubator. Prior to cocultivation, P-DN hydrogel samples underwent ultraviolet (UV) light exposure for 1 h, followed by sterilization through immersion in 75% ethanol for 20 min. The samples were then immersed in phosphate-buffered saline (PBS) solution for 60 min, with the PBS being refreshed every 20 min. Subsequently, the P-DN hydrogel samples were immersed in DMEM culture medium containing 10% FBS for 20 min to facilitate the trypsinization and resuspension of Saos-2 cells. The cells were seeded in the confocal culture dishes at a density of 1.0×10^5 cells/ml. For the experimental group, Saos-2 cells were cocultured with P-DN hydrogel samples for a duration of 3 days. A control group was also established by seeding cells at the same density in confocal culture dishes under the same incubation conditions as the experimental group. At 24, 48, and 72 h, the experimental and control groups were stained with Calcein AM/PI to distinguish live from dead cells. We processed the fluorescence images from the cocultivation experiments of the experimental and control groups, comparing images from three different regions at three different times for both groups. The number of live cells (green fluorescence) and dead cells (red fluorescence) was counted using a cell counting tool (ImageJ NIH) to calculate the cell viability in each region. The survival rate was calculated as [(number of live cells/(number of live cells + number of dead cells)) × 100%].

Fabrication of Planar Fluidic Channel Devices. A system designed for the collection and amplification of signals was constructed using PEGDA and 3D printing technology. The system comprises three interconnected cylindrical chambers, each with a diameter of 2 mm and a height of 3 mm, a hydrogel plate featuring a 1.5 mm aperture and 1 mm in thickness, and a 0.5 mm thick hydrogel membrane. The hydrogel membrane was utilized to seal one side of the cylindrical chambers. Following this, silicone oil was infused into all chambers and channels within the framework, and a 1.5 mm thick hydrogel plate was affixed to the opposite side of the chambers. The polymerization process was executed by uniformly coating each component with PEGDA bioink and subsequently curing it under ultraviolet light to ensure the integrity of the system and prevent silicone oil leakage during experimental procedures.

Manufacture of Models of Liquid Filling Chambers. The liquid filling chamber model was constructed as a rectangular PEGDA hydrogel structure with dimensions of 30 mm in length, 10 mm in width, and 10 mm in height, incorporating three cylindrical cavities measuring 2 mm in diameter and 5 mm in height. A hydrogel plate, 1 mm in thickness, was perforated with apertures of 1, 1.5, and 2 mm in diameter to function as a cover for the cavities, and a grating membrane was utilized to seal these apertures. The hydrogel solution was employed to bond the cylindrical chamber model with the hydrogel plate, which was then cured using an ultraviolet (UV) lamp to ensure the prevention of any leakage. Furthermore, a small hole was drilled into the side of the cylindrical chamber model to allow for the insertion of a syringe pump, designed to regulate internal pressure by introducing a flowing fluid from an external source.

Physicochemical Properties of Oxygen Permeability, Water Content, Hydrophilicity and Elastic Modulus of P-DN Hydrogel Contact Lenses. Our smart contact lens, when worn on the cornea, features a nonfull-coverage, hollow structure, ensuring proper oxygen permeability during IOP monitoring. Also, contact lenses are generally stored in water. As per eq 3, water content is determined by fully water-swelling the smart contact lens, then drying it. It is calculated by subtracting the dry mass from the swollen mass and dividing by the swollen mass.

$$WC = \frac{w_{wet} - w_{dry}}{w_{wet}} \times 100\% \quad (3)$$

As shown in Figure S15, our contact lenses have a water content of about 53.33%, close to the 55% of commercial ones. This indicates that P-DN hydrogel is suitable for making smart contact lenses. Additionally, we assessed the hydrophilicity of P-DN and commercial contact lenses using a contact angle goniometer. The P-DN lenses had a contact angle of roughly 23°, compared to 25° for the commercial lenses. Figure S16 shows the contact angle comparison from multiple experiments. Our P-DN contact lenses demonstrated a smaller contact angle, indicating better hydrophilicity than commercial lenses. As shown in Figure S17, after subjecting the P-DN hydrogel to tensile testing and analyzing the data, we determined its elastic modulus to be 1.26 MPa. This value lies within the required range of 0.43−1.52 MPa[47] for commercial contact lenses, indicating that our P-DN contact lenses meet the manufacturing standards.

ASSOCIATED CONTENT

Supporting Information

The Supporting Information is available free of charge at https://pubs.acs.org/doi/10.1021/acssensors.5c00883.

3D printing equipment, corneal fitting experiment, optimal aperture test diagram and experimental setup diagram, micro binocular camera, best starting color analysis, hydrogel material structure and surface roughness experiment (PDF)

https://doi.org/10.1021/acssensors.5c00883
ACS Sens. XXXX, XXX, XXX−XXX

AUTHOR INFORMATION

Corresponding Authors

Tingting Luo − *School of Biomedical Engineering, 3D-Printing and Tissue Engineering Center, Anhui Medical University, Hefei 230032, China;* orcid.org/0009-0000-8503-1831; Email: luotingting@ahmu.edu.cn

Guangli Liu − *School of Biomedical Engineering, 3D-Printing and Tissue Engineering Center, Anhui Medical University, Hefei 230032, China*; Email: liuguangli@ahmu.edu.cn

Yijing Gan − *Department of Ophthalmology, The First Affiliated Hospital of University of Science and Technology of China, Hefei 230036, China*; Email: yijinggan@outlook.com

Runhuai Yang − *School of Biomedical Engineering, 3D-Printing and Tissue Engineering Center, Anhui Medical University, Hefei 230032, China;* orcid.org/0000-0002-3529-0277; Email: yangrunhuai@ahmu.edu.cn

Authors

Yunhao Tai − *School of Biomedical Engineering, 3D-Printing and Tissue Engineering Center, Anhui Medical University, Hefei 230032, China*

Qilong Cheng − *School of Biomedical Engineering, 3D-Printing and Tissue Engineering Center, Anhui Medical University, Hefei 230032, China*

Yuteng Liu − *School of Biomedical Engineering, 3D-Printing and Tissue Engineering Center, Anhui Medical University, Hefei 230032, China*

Xingqi Lu − *School of Biomedical Engineering, 3D-Printing and Tissue Engineering Center, Anhui Medical University, Hefei 230032, China*

Ting Xu − *School of Biomedical Engineering, 3D-Printing and Tissue Engineering Center, Anhui Medical University, Hefei 230032, China*

Xiaojian Li − *Key Laboratory of Process Optimization and Intelligent Decision-making, School of Management, Hefei University of Technology, Hefei 230009, China*

Ping Liu − *Sensitive Electronics and Sensors Research Group, School of Electronic Science and Applied Physics, Hefei University of Technology, Hefei 230009, China;* orcid.org/0000-0002-0330-0100

Complete contact information is available at: https://pubs.acs.org/10.1021/acssensors.5c00883

Author Contributions

Y−H.T.: methodology, visualization, writing-original draft. Q-L.C.: methodology. Y-T.L.: methodology, investigation. X-Q.L.: formal analysis, review. T.X.: investigation. X-J.L.: investigation. P.L.: investigation. T−T.L.: methodology and supervision, project administration. G-L.L.: methodology and supervision, project administration. Y-J.G.: methodology and supervision, project administration. R−H.Y.: project administration, funding acquis-ition and visualization. All authors have given approval to the final version of the manuscript.

Notes

The authors declare no competing financial interest.

ACKNOWLEDGMENTS

This work was supported by the National Natural Science Foundation of China (Nos. 62373004,61973003), the Technical development project of Anhui Medical University (2022100, 2022054, 2023045),the Outstanding Youth Research Project in Universities of Anhui Province (2022AH030077), the Scientific research improvement Foundation of Anhui Medical University (2023xkjT002), the "Four New" Research and Reform Practice Project (Emerging Engineering Education) of Anhui Province (2023sx030), Anhui Provincial Major Science and Technology Project (202203a05020010).

REFERENCES

(1) Liu, W.; Du, Z.; Duan, Z.; Li, L.; Shen, G. Neuroprosthetic contact lens enabled sensorimotor system for point-of-care monitoring and feedback of intraocular pressure. *Nat. Commun.* **2024**, *15* (1), 5635.

(2) Zhang, J.; Kim, K.; Kim, H. J.; Meyer, D.; Park, W.; Lee, S. A.; Dai, Y.; Kim, B.; Moon, H.; Shah, J. V.; Harris, K. E.; Collar, B.; Liu, K.; Irazoqui, P.; Lee, H.; Park, S. A.; Kollbaum, P. S.; Boudouris, B. W.; Lee, C. H. Smart soft contact lenses for continuous 24-hour monitoring of intraocular pressure in glaucoma care. *Nat. Commun.* **2022**, *13* (1), 5518.

(3) Ho, C. H.; Wong, J. K. W. Role of 24-h Intraocular Pressure Monitoring in Glaucoma Management. *J. Ophthalmol* **2019**, *2019*, 3632197.

(4) Maeng, B.; Chang, H. K.; Park, J. Photonic crystal-based smart contact lens for continuous intraocular pressure monitoring. *Lab Chip* **2020**, *20* (10), 1740−1750.

(5) Yang, C.; Huang, X.; Li, X.; Yang, C.; Zhang, T.; Wu, Q.; Liu, D.; Lin, H.; Chen, W.; Hu, N.; Xie, X. Wearable and Implantable Intraocular Pressure Biosensors: Recent Progress and Future Prospects. *Adv. Sci. (Weinh)* **2021**, *8* (6), 2002971.

(6) Naidana, K. S.; Manne, M. H.; Yalavarthi, H. A deep retinal vision network for glaucoma classification. *Discov. Appl. Sci* **2025**, *7* (3), 175.

(7) Celik, G.; Karacocuk, T.; Ciftci, F. Evaluation of additional points in the 24−2C visual field test in pre-perimetric glaucoma. *Photodiagnosis Photodyn Ther* **2025**, *52*, 104513.

(8) An, H.; Wang, X.; Liao, Z.; Zhang, L.; Zhao, H.; Yang, Y.; Song, J.; Ma, Y. LC contact lens sensor for ultrasensitive intraocular pressure monitoring. *npj Flexible Electronics* **2024**, *8* (1), 53.

(9) Kobashi, H.; Kobayashi, M. 3D-printed eye model: Simulation of intraocular pressure. *PLoS One* **2023**, *18* (3), No. e0282911.

(10) Li, X.; Chen, W.; Li, H.; Shen, B.; He, J.; Gao, H.; Bin, F.; Li, H.; Xiao, D. Temperature Self-Compensating Intelligent Wireless Measuring Contact Lens for Quantitative Intraocular Pressure Monitoring. *ACS Appl. Mater. Interfaces* **2024**, *16* (17), 22522−22531.

(11) Lin, Y.; Xiang, S.; Zou, W.; Chen, X.; Gao, F.; Liu, Y.; Sun, Y.; Chen, P.; Zhang, Q.; Han, X.; Wang, B.; Yao, Y.; Shi, Q.; Wu, J. Magneto-elastic for wireless intraocular pressure monitoring. *Chem. Eng. J.* **2024**, *498*, 155357.

(12) Ren, X.; Zhou, Y.; Lu, F.; Zhai, L.; Wu, H.; Chen, Z.; Wang, C.; Zhu, X.; Xie, Y.; Cai, P.; Xu, J.; Tang, X.; Li, J.; Yao, J.; Jiang, Q.; Hu, B. Contact Lens Sensor with Anti-jamming Capability and High Sensitivity for Intraocular Pressure Monitoring. *ACS Sensors* **2023**, *8* (7), 2691−2701.

(13) Wasilewicz, R.; Varidel, T.; Simon-Zoula, S.; Schlund, M.; Cerboni, S.; Mansouri, K. First-in-human continuous 24-h measurement of intraocular pressure and ocular pulsation using a novel contact lens sensor. *Br J. Ophthalmol* **2020**, *104* (11), 1519−1523.

(14) Xu, J.; Cui, T.; Hirtz, T.; Qiao, Y.; Li, X.; Zhong, F.; Han, X.; Yang, Y.; Zhang, S.; Ren, T. L. Highly Transparent and Sensitive Graphene Sensors for Continuous and Non-invasive Intraocular Pressure Monitoring. *ACS Appl. Mater. Interfaces* **2020**, *12* (16), 18375−18384.

(15) Zhu, H.; Yang, H.; Xu, S.; Ma, Y.; Zhu, S.; Mao, Z.; Chen, W.; Hu, Z.; Pan, R.; Xu, Y.; Xiong, Y.; Chen, Y.; Lu, Y.; Ning, X.; Jiang, D.; Yuan, S.; Xu, F. Frequency-encoded eye tracking smart contact lens for human-machine interaction. *Nat. Commun.* **2024**, *15* (1), 3588.

(16) Liu, Z.; Wang, G.; Pei, W.; Wei, C.; Wu, X.; Dou, Z.; Li, Y.; Wang, Y.; Chen, H. Application of graphene nanowalls in an intraocular pressure sensor. *J. Mater. Chem. B* **2020**, *8* (38), 8794−8802.
(17) Minami, K.; Yaguchi, S.; Bissen-Miyajima, H. Temperature-controlled porcine eye holder for observing intraocular temperature during cataract surgery. *Sci. Rep.* **2023**, *13* (1), 4331.
(18) M Kouhani, M. H.; Wu, J.; Tavakoli, A.; Weber, A. J.; Li, W. Wireless, passive strain sensor in a doughnut-shaped contact lens for continuous non-invasive self-monitoring of intraocular pressure. *Lab Chip* **2020**, *20* (2), 332−342.
(19) Zhang, Y.; Wu, L.; Zou, M.; Zhang, L.; Song, Y. Suppressing the Step Effect of 3D Printing for Constructing Contact Lenses. *Adv. Mater.* **2022**, *34* (4), No. e2107249.
(20) Yang, C.; Wu, Q.; Liu, J.; Mo, J.; Li, X.; Yang, C.; Liu, Z.; Yang, J.; Jiang, L.; Chen, W.; Chen, H. J.; Wang, J.; Xie, X. Intelligent wireless theranostic contact lens for electrical sensing and regulation of intraocular pressure. *Nat. Commun.* **2022**, *13* (1), 2556.
(21) Kim, J.; Kim, M.; Lee, M. S.; Kim, K.; Ji, S.; Kim, Y. T.; Park, J.; Na, K.; Bae, K. H.; Kyun Kim, H.; Bien, F.; Young Lee, C.; Park, J. U. Wearable smart sensor systems integrated on soft contact lenses for wireless ocular diagnostics. *Nat. Commun.* **2017**, *8*, 14997.
(22) Zhang, H.; Wang, C.; Bai, M.; Yi, H.; Yang, J.; Zhu, Y.; Zhao, J. A Micro-3-Degree-of-Freedom Force Sensor for Intraocular Dexterous Surgical Robots. *Adv. Intell. Syst* **2023**, *5* (7), 2200413.
(23) Duan, Z.; Yuan, M.; Liu, Z.; Pei, W.; Jiang, K.; Li, L.; Shen, G. An Ultrasensitive $Ti_3C_2T_x$ MXene-based Soft Contact Lens for Continuous and Nondestructive Intraocular Pressure Monitoring. *Small* **2024**, *20* (24), No. e2309785.
(24) Zhu, H.; Yang, H.; Zhan, L.; Chen, Y.; Wang, J.; Xu, F. Hydrogel-Based Smart Contact Lens for Highly Sensitive Wireless Intraocular Pressure Monitoring. *ACS Sensors* **2022**, *7* (10), 3014−3022.
(25) Zolfaghari, P.; Yalcinkaya, A. D.; Ferhanoglu, O. Smart glasses to monitor intraocular pressure using optical triangulation. *Opt. Commun.* **2023**, *546*, 129752.
(26) Cheng, Y.; Zhan, Y.; Guan, F.; Shi, J.; Wang, J.; Sun, Y.; Zubair, M.; Yu, C.; Guo, C. F. Displacement-pressure biparametrically regulated softness sensory system for intraocular pressure monitoring. *Natl. Sci. Rev.* **2024**, *11* (6), nwae050.
(27) Kalyuzhner, Z.; Agdarov, S.; Beiderman, Y.; Bennet, A.; Beiderman, Y.; Zalevsky, Z. Remote and low-cost intraocular pressure monitoring by deep learning of speckle patterns. *J. Biomed Opt* **2024**, *29* (3), 037003.
(28) Zhang, Y.; Chen, Y.; Man, T.; Huang, D.; Li, X.; Zhu, H.; Li, Z. High resolution non-invasive intraocular pressure monitoring by use of graphene woven fabrics on contact lens. *Microsyst Nanoeng* **2019**, *5*, 39.
(29) Liu, Z.; Wang, G.; Ye, C.; Sun, H.; Pei, W.; Wei, C.; Dai, W.; Dou, Z.; Sun, Q.; Lin, C. T.; Wang, Y.; Chen, H.; Shen, G. An Ultrasensitive Contact Lens Sensor Based On Self-Assembly Graphene For Continuous Intraocular Pressure Monitoring. *Adv. Funct. Mater.* **2021**, *31* (29), 2010991.
(30) Yang, H.; Zhu, H.; Liu, H.; Mao, Z.; Luo, J.; Zhu, S.; Hu, Z.; Yuan, S.; Xu, F. Intraocular Pressure Monitoring Smart Contact Lens with High Environmental Stability. *Adv. Funct. Mater.* **2024**, *34* (34), 2400722.
(31) Kim, J.; Kim, J.; Ku, M.; Cha, E.; Ju, S.; Park, W. Y.; Kim, K. H.; Kim, D. W.; Berggren, P. O.; Park, J. U. Intraocular Pressure Monitoring Following Islet Transplantation to the Anterior Chamber of the Eye. *Nano Lett.* **2020**, *20* (3), 1517−1525.
(32) Xie, M.; Yao, G.; Zhang, T.; Wang, Q.; Mo, X.; Dong, Q.; Lou, W.; Lu, F.; Pan, T.; Gao, M.; Jiang, D.; Zhao, K.; Lin, Y. Multifunctional flexible contact lens for eye health monitoring using inorganic magnetic oxide nanosheets. *J. Nanobiotechnol.* **2022**, *20* (1), 202.
(33) Liao, J.; Ye, C.; Guo, J.; Garciamendez-Mijares, C. E.; Agrawal, P.; Kuang, X.; Japo, J. O.; Wang, Z.; Mu, X.; Li, W.; Ching, T.; Mille, L. S.; Zhu, C.; Zhang, X.; Gu, Z.; Zhang, Y. S. 3D-printable colloidal photonic crystals. *Mater. Today* **2022**, *56*, 29−41.
(34) McMonnies, C. W.; Boneham, G. C. Corneal curvature stability with increased intraocular pressure. *Eye Contact Lens* **2007**, *33* (3), 130−137.
(35) Kim, T. Y.; Mok, J. W.; Hong, S. H.; Jeong, S. H.; Choi, H.; Shin, S.; Joo, C.-K.; Hahn, S. K. Wireless theranostic smart contact lens for monitoring and control of intraocular pressure in glaucoma. *Nat. Commun.* **2022**, *13* (1), 6801.
(36) Asrani, S. G.; McGlumphy, E. J.; Al-Aswad, L. A.; Chaya, C. J.; Lin, S.; Musch, D. C.; Pitha, I.; Robin, A. L.; Wirostko, B.; Johnson, T. V. The relationship between intraocular pressure and glaucoma: An evolving concept. *Prog. Retin Eye Res.* **2024**, *103*, 101303.
(37) Biswas, S.; Biswas, P. Relationship between Diurnal Variation in Intraocular Pressure and Central Corneal Power. *Optom Vis Sci.* **2023**, *100* (1), 96−104.
(38) Da Silva, F.; Lira, M. Intraocular pressure measurement: A review. *Surv Ophthalmol* **2022**, *67* (5), 1319−1331.
(39) Zhang, W.; Huang, L.; Weinreb, R. N.; Cheng, H. Wearable electronic devices for glaucoma monitoring and therapy. *Mater. Des.* **2021**, *212*, 110183.
(40) Liu, W.; Du, Z.; Duan, Z.; Liu, H.; Li, L.; Jiang, K.; Chen, D.; Shen, G. Eye-wearable Ti3C2Tx MXene-based micro-supercapacitor as a power unit for intraocular pressure applications. *J. Mater. Chem. A* **2024**, *12* (27), 16457−16465.
(41) Ma, H.; Liu, Z.; Lu, X.; Zhang, S.; Tang, C.; Cheng, Y.; Zhang, H.; Liu, G.; Sui, C.; Ding, C.; Yang, R.; Luo, T. 3D printed multi-coupled bioinspired skin-electronic interfaces with enhanced adhesion for monitoring and treatment. *Acta Biomater.* **2024**, *187*, 183−198.
(42) Branisteanu, D. C.; Moraru, A. D.; Maranduca, M. A.; Branisteanu, D. E.; Stoleriu, G.; Branisteanu, C. I.; Balta, F. Intraocular pressure changes during and after silicone oil endotamponade. *Exp Ther Med.* **2020**, *20* (6), 204.
(43) Dennyson Savariraj, A.; Salih, A.; Alam, F.; Elsherif, M.; AlQattan, B.; Khan, A. A.; Yetisen, A. K.; Butt, H. Ophthalmic Sensors and Drug Delivery. *ACS Sens* **2021**, *6* (6), 2046−2076.
(44) Kang, K.; Park, J.; Kim, K.; Yu, K. J. Recent developments of emerging inorganic, metal and carbon-based nanomaterials for pressure sensors and their healthcare monitoring applications. *Nano Res.* **2021**, *14* (9), 3096−3111.
(45) Li, Y.; Li, L.; Ye, Z.; Zhang, H.; Sun, X.; Li, C.; Gui, L. A Novel Implantable Piezoresistive Microsensor for Intraocular Pressure Measurement. *ACS Sens* **2024**, *9* (8), 3958−3966.
(46) Lim, J.; Lee, H.; Kim, J.; Moon, C. E.; Lee, J. K.; Kang, Y.; Kim, R.; Mun, B.; Ji, Y. W.; Haam, S. Implantable Intraocular Fluorescence Sensor for Visualized Monitoring of Alzheimer's Disease. *Adv. Funct. Mater.* **2024**, *35* (3), 2413723.
(47) Chen, Y.; Li, D.; Chen, Y.; Fang, H. Polyethylene Glycol Diacrylate Adapted Photopolymerization Material for Contact Lens with Improved Elastic Modulus Properties. *Materials (Basel)* **2025**, *18* (4), 827.

https://doi.org/10.1021/acssensors.5c00883
ACS Sens. XXXX, XXX, XXX−XXX